



ELSEVIER

Nuclear Instruments and Methods in Physics Research A 440 (2000) 263–284

**NUCLEAR  
INSTRUMENTS  
& METHODS  
IN PHYSICS  
RESEARCH**  
Section A

www.elsevier.nl/locate/nima

## The bremsstrahlung tagged photon beam in Hall B at JLab

D.I. Sober<sup>a</sup>, Hall Crannell<sup>a</sup>, Alberto Longhi<sup>a</sup>, S.K. Matthews<sup>a,1</sup>, J.T. O'Brien<sup>a,\*</sup>,  
B.L. Berman<sup>b</sup>, W.J. Briscoe<sup>b</sup>, Philip L. Cole<sup>b,2</sup>, J.P. Connelly<sup>b,3</sup>, W.R. Dodge<sup>b</sup>,  
L.Y. Murphy<sup>b</sup>, S.A. Philips<sup>b</sup>, M.K. Dugger<sup>c</sup>, D. Lawrence<sup>c,4</sup>, B.G. Ritchie<sup>c</sup>,  
E.S. Smith<sup>d</sup>, James M. Lambert<sup>e</sup>, E. Anciant<sup>f</sup>, G. Audit<sup>f</sup>, T. Auger<sup>f</sup>, C. Marchand<sup>f</sup>,  
M. Klusman<sup>g</sup>, J. Napolitano<sup>g</sup>, M.A. Khandaker<sup>h</sup>, C.W. Salgado<sup>h</sup>, A.J. Sarty<sup>i</sup>

<sup>a</sup>Department of Physics, The Catholic University of America, Washington, DC 20064, USA

<sup>b</sup>Center for Nuclear Studies, Department of Physics, The George Washington University, Washington, DC 20052, USA

<sup>c</sup>Department of Physics and Astronomy, Arizona State University, Tempe, AZ 85287-1504, USA

<sup>d</sup>The Thomas Jefferson National Accelerator Facility, Newport News, VA 23606, USA

<sup>e</sup>Department of Physics, Georgetown University, Washington, DC 20057, USA

<sup>f</sup>Service de Physique Nucléaire, DAPNIA/DSM, CEA-Saclay, France

<sup>g</sup>Department of Physics, Applied Physics and Astronomy, Rensselaer Polytechnic Institute, Troy, NY 12180-3590, USA

<sup>h</sup>Department of Physics, Norfolk State University, Norfolk, VA 23504, USA

<sup>i</sup>Department of Physics, Florida State University, Tallahassee, FL 32306-3016, USA

Received 17 May 1999; accepted 17 July 1999

### Abstract

We describe the design and commissioning of the photon tagging beamline installed in experimental Hall B at the Thomas Jefferson National Accelerator Facility (JLab). This system can tag photon energies over a range from 20% to 95% of the incident electron energy, and is capable of operation with beam energies up to 6.1 GeV. A single dipole magnet is combined with a hodoscope containing two planar arrays of plastic scintillators to detect energy-degraded electrons from a thin bremsstrahlung radiator. The first layer of 384 partially overlapping small scintillators provides photon energy resolution, while the second layer of 61 larger scintillators provides the timing resolution necessary to form a coincidence with the corresponding nuclear interaction triggered by the tagged photon. The definitions of overlap channels in the first counter plane and of geometric correlation between the two planes are determined using digitized time information from the individual counters. Auxiliary beamline devices are briefly described, and performance results to date under real operating conditions are presented. The entire photon-tagging system has met or exceeded its design goals. © 2000 Elsevier Science B.V. All rights reserved.

\*Corresponding author. Permanent address: Montgomery College, Rockville, MD 20850, USA. Tel.: +1-202-319-5319; fax: +1-202-319-4448.

E-mail address: obrienj@cua.edu (J.T. O'Brien)

<sup>1</sup>Current address: Oregon Hearing Research Center, Portland, OR 97201-3098, USA.

<sup>2</sup>Current address: Department of Physics, University of Texas at El Paso, El Paso, TX 79968, USA.

<sup>3</sup>Current address: Cisco Systems, Herndon, VA 20171, USA.

<sup>4</sup>Current address: Department of Physics, University of Massachusetts, Amherst, MA 01003, USA.

PACS: 29.30.Kv; 29.40.Mc; 29.70.Fm

Keywords: CLAS; Photon tagger; Photon beam; Scintillator hodoscope; Time-based logic

## 1. Introduction

We report the design, construction, and commissioning of the photon-tagging system now in use in Hall B at the Thomas Jefferson National Accelerator Facility (JLab) for the investigation of real-photon-induced reactions. The tagger was initially designed to be used in conjunction with the CEBAF (Continuous Electron Beam Accelerator Facility) Large Acceptance Spectrometer (CLAS) [1], and has subsequently also been used in two additional experiments which do not make use of CLAS. While the descriptions in this paper make frequent reference to correlations of tagger information with the CLAS detector, it is intended that the reader understand that all such discussions have equivalent application to any other downstream detector system for photon-induced interactions.

The bremsstrahlung tagging technique for direct measurement of incident photon energy in photo-nuclear interactions is well established [2–4]. The

JLab system is the first photon tagger in the multi-GeV energy range to combine high resolution ( $\sim 10^{-3}E_0$ ) with a broad tagging range (20–95% of  $E_0$ ).

## 2. Background and general description

The geometry of our system is sketched in Fig. 1, with additional, more detailed views in Figs. 2 and 3. Electrons from the CEBAF accelerator strike a thin target (the “radiator”) just upstream from a magnetic spectrometer (the “tagger”). The system is based upon the electron bremsstrahlung reaction in which an electron of incident energy  $E_0$  is “decelerated” (scattered) by the electromagnetic field of a nucleus, and in the process emits an energetic photon (gamma ray). The energy transferred to the nucleus is negligibly small, so the reaction obeys the energy conservation relation

$$E_\gamma = E_0 - E_e$$

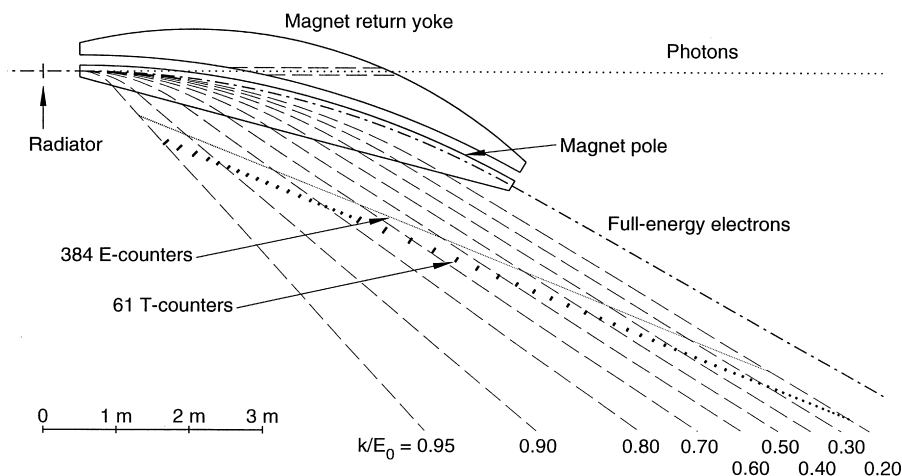


Fig. 1. Overall geometry of tagging system. Important details referenced in the text include the shape of the magnet pole, the straight-ahead photon path through the magnet yoke, and the relative locations of the hodoscope  $E$ - and  $T$ -planes. Also shows “typical” electron trajectories labeled according to the fraction of the incident energy that was transferred to the photon.

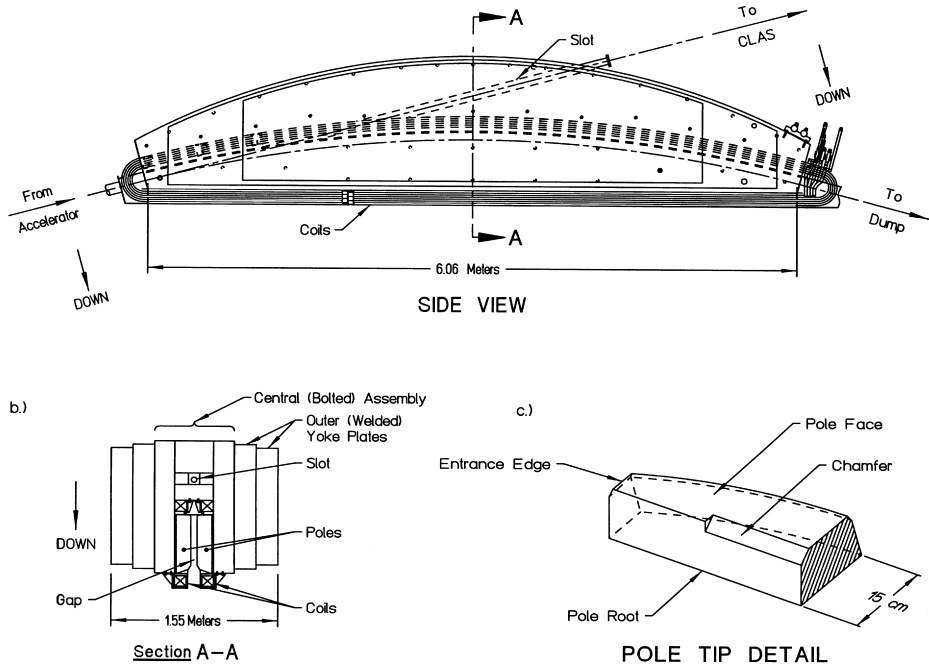


Fig. 2. Views of the assembled tagger magnet; (a) is a side elevation, showing such details as yoke plate profiles, straight-ahead vacuum pipe through yoke, coil shape and location; (b) is a central transverse section which shows the laminar construction of the yoke as well as additional detail on relative positions of poles, coils, and vacuum walls; (c) is an isometric sketch of the entrance tip of one pole, showing pole nomenclature used in the text, and some details of pole chamfers and cross section.

where  $E_e$  is the energy of the outgoing electron and  $E_\gamma$  is the energy of the emitted photon. Since  $E_0$  is uniquely determined by the accelerator, a measurement of the outgoing electron energy by a magnetic spectrometer thus provides a determination of the photon energy.

At energies above a few MeV, the outgoing electron and photon emerge at very small angles relative to the incident beam direction. The angular distribution of the photons has a characteristic angle

$$\theta_c = mc^2/E_0$$

where  $m$  is the electron rest mass, while the electron's characteristic angle is given by

$$\theta_e = \theta_c E_\gamma/E_e.$$

At Jefferson Lab energies ( $> 800$  MeV), both of these angles are of order 1 mr or smaller, so that in first approximation both the photon and the elec-

tron are still traveling along the original beam direction.

Any photons which are produced in the radiator thus continue straight ahead through the tagger magnet, toward the target farther downstream in the experimental hall upon which photon-induced reactions are to be studied. A collimation system to further define the photon beam is positioned just downstream of the tagger, centered on the photon beamline. This system, which is indicated in Fig. 3, has two sets of interchangeable collimator inserts, with interspaced sweep magnets to clean up any charged particle background generated in the collimator walls.

The field setting of the tagger magnet is matched to the incident beam energy so that those electrons which do not radiate will follow a circular arc just inside the curved edge of the pole face, and will be directed into a shielded beam dump below the floor of the experimental hall. Electrons which do give up

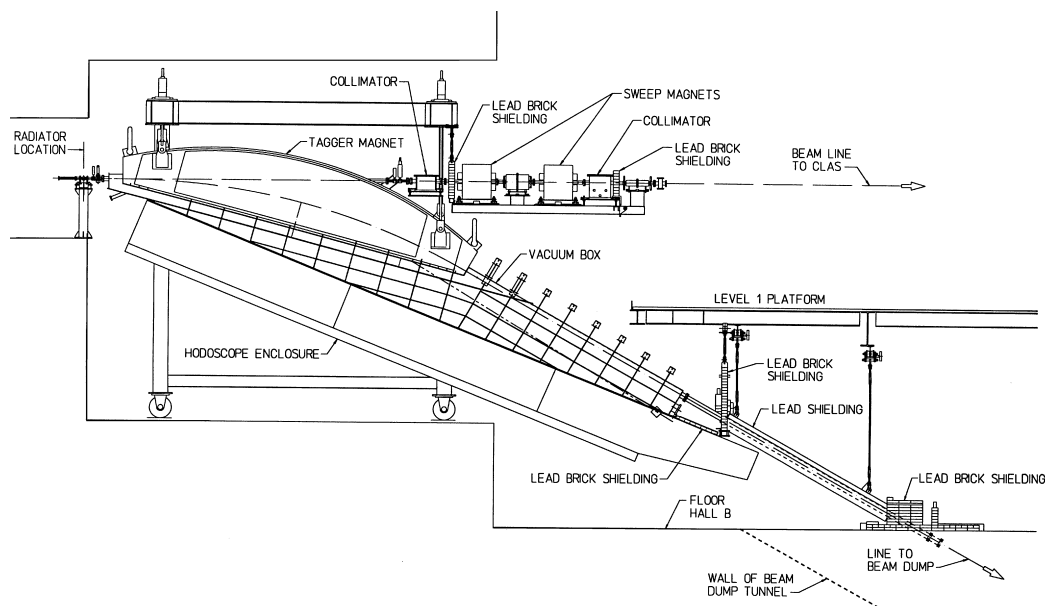


Fig. 3. Elevation view of the assembled system and gantry standing in the alcove. As a scale reference, the overall length of the tagger magnet is  $\sim 6$  m. Important details include the ribbed vacuum box, location of radiator, hodoscope enclosure, collimators, shielding, and beam dump entrance.

energy to generate a bremsstrahlung photon experience greater curvature in the tagger field, and emerge from the magnet somewhere along the straight edge of the pole gap. A scintillator hodoscope along the flat focal plane downstream from this straight edge detects these energy-degraded electrons, and thereby allows for the determination of the energy of the radiated photon. This hodoscope must have adequate segmentation to deliver the desired energy resolution. Its instrumentation must also provide timing information sufficiently precise to allow for correlation with a particular nuclear interaction in the downstream target to within the 2 ns interval between beam “buckets” from the accelerator.

Electrons must be transported to the detectors in vacuum, in order to minimize the effects of multiple scattering on the achievable energy resolution. As it was considered impractical to locate such a large detector system inside a vacuum chamber, it was necessary to have a thin exit window located as close as practical to the detector plane. The vacuum window covers an aperture of  $9.6 \text{ m} \times 20 \text{ cm}$ , and is composed of aluminized Mylar backed by Kevlar

cloth, with a combined average thickness of  $\sim 6 \times 10^{-4}$  radiation lengths. Construction and installation details of this thin vacuum window have already been presented in an earlier publication [5].

In the sections which follow, we discuss the optical design of the magnet, structural details of the magnet, vacuum, and hodoscope assemblies, and the details of our electronics readout scheme. We provide brief descriptions of various auxiliary beam-line devices, and we report on the performance of the system during its early running period.

### 3. The magnet

#### 3.1. Optical design

The desire for the largest practical dynamic range – photon energies from  $\sim 20\%$  to  $\sim 95\%$  of the initial electron energy – required an open-yoke geometry that would permit such a large range of orbit radii to reach the detector array. A goal to achieve energy resolution of  $\sim 10^{-3} E_0$  placed

requirements on field uniformity, and argued strongly in favor of a design with a relatively simple focal surface. Finally, a strong interest in the possibility of future expansion to use electron/photon out-of-plane angular correlations for identification of photon linear polarization demanded magnet optics that would preserve the transverse angle information for the electron, and would optimally map this distribution onto the focal surface.

The optical design of the tagger magnet was done at Catholic University [6]. The final design is a modified Elbek spectrometer [7] – a single, uniform-field dipole with a total deflection angle of  $30^\circ$ , the smallest angle that would allow a sensible placement of the beam dump. A magnet with a larger deflection angle would have been superior from the standpoint of optics, but much heavier and more expensive to build.

At the time that this design was finalized, the approved upper limit for the CEBAF accelerator was 4 GeV, a beam energy that is very comfortably within the capabilities of this magnet. The as-built design, with the present power supply, will in fact allow operation at up to  $\sim 6$  GeV with somewhat degraded field uniformity. Planning for possible future upgrades of CEBAF toward operation at that energy, and perhaps beyond, has indeed been subsequently authorized.

The defining characteristic of an Elbek magnet is a uniform magnetic field configured so that the exit field boundary is a straight edge which projects back to the point at which the incident particle enters the field. Outgoing trajectories are parallel, and the bend-plane images lie along a plane outside the field. A particularly simple pole face geometry for such a magnet would be a segment of a circle, with particles both entering and leaving across the straight (chord) edge.

This basic shape was adapted, by trimming off the sharp points at either end, to produce the pole profile shown in Fig. 1. This adjustment modified the optics in three significant ways:

- a. The projection of the long exit edge now intercepts the incident trajectory somewhat upstream from its entrance into the field. This effectively rotates the edge slightly from a true Elbek configuration, and increases the path length inside

the field for the lower-energy electrons. This has the advantage of moving the low-momentum end of the image plane farther away from the field boundary, providing more space for installation of detectors. With this pole shape the exit trajectories are no longer parallel, but the image surface is still essentially a plane.

- b. The incident electron beam now crosses normal to the local field boundary.
- c. The full-energy exit beam also crosses normal to the local field boundary, so that the full-energy trajectories into the beam dump are more nearly parallel. Since this shortens the total path length of such trajectories inside the field, the deflection angle for full-energy electrons is now a few degrees smaller than would be the case along the unmodified Elbek shape.

The spectrometer magnetic field is defocusing in the transverse plane, so that a beam spot on the radiator will be imaged to a line in the detector plane. This property is potentially useful in seeking to select polarization by angular correlation as mentioned above, since transverse position at the image plane is proportional to transverse angle at the radiator. This effect could be enhanced by displacing the radiator upstream from its nominal position of 50 cm from the field entry edge, which can be done without seriously degrading the energy resolution. However, there are no longer any plans to instrument this particular polarization option at the time of this writing.

The shaping of the pole edges and the dimensions of the return yoke were designed using the two-dimensional magnetic field program POISSON [8]. Because of the elongated shape of the magnet, it was reasonable to approximate the magnet in two dimensions by using pole cross sections at the midpoint and at three other positions between the center and the end. At each of these positions, the cross section of the return yoke was adjusted until the saturation curves at the four positions were equal and provided satisfactory fields up to 1.75 T (the field value required to transport a 6 GeV beam along the full-energy orbit to the beam dump). The curvature of the designed return yoke was determined by a fit to these four calculated values.

POISSON calculations were also used in designing the cross-section profile of the magnet pole (the hatched surface in Fig. 2c). A two-step linear contour was used as a starting configuration, and the shape was adjusted slightly to minimize saturation effects and to make the effective field boundary coincide with the edge of the pole root. The inner chamfer did not extend all the way to the ends of the long exit edge (see Fig. 2c), where the pole width was only  $\sim 15$  cm, so as not to interfere with the field uniformity at the entry edge and the full-energy exit edge of the magnet.

### 3.2. Magnet and vacuum specifications

Structural and assembly design for the magnet, vacuum system, and related mechanical components was developed at Catholic University and refined by the Jefferson Lab engineering staff. Two views of the assembled magnet are shown in Fig. 2. It is topologically a C-magnet, with the yoke completely open along the straight edge to allow free passage for degraded electrons along this entire length.

The magnet has a full-energy radius of curvature of 11.80 m and deflection angle of  $30^\circ$ . It is 6.06 m in length along the open chord, has a gap width of 5.7 cm, and weighs  $\sim 68\,000$  kg. Pole width is  $\sim 0.5$  m at the midpoint, tapering to 0.16 m at the ends. A typical magnetic field in the gap is 1.13 T for a beam energy of 4 GeV.

The gap width of 5.7 cm was determined by the criterion that the lowest-energy electrons at an incident energy of 800 MeV (the lowest anticipated beam energy at JLab) should be detected with 90% efficiency. A narrower gap would have unacceptably encroached upon the production cone for these electrons. The pole faces are themselves incorporated as the side walls of the vacuum containment, primarily because any separate vacuum chamber with walls thick enough to be self-supporting would have required an enlargement of the gap (with associated upscaling of other design parameters) in order to preserve this clearance.

The magnet yoke is built up in a laminar fashion (see Fig. 2b) from seven separate steel plates that were cut and machined by outside vendors and were then assembled on site at JLab. They are

made from AISI 1006 steel, which is a very low carbon steel (0.06%) with essentially no other alloy content. The three innermost layers, which form an integral assemblage with the pole tip, coil, and vacuum structures, are precision machined on all mating faces to control for the ultimate uniformity of the magnet gap. The major components in this central group are bolted together, to allow for pole gap alignment, vacuum welding, and coil installation. The two outermost yoke layers on either side, which were torch-cut from rolled plates by the supplier with almost no finish machining, were simply tack-welded to the central assembly around their perimeters at the completion of the assembly process.

The mid-plane layer is of double thickness (36 cm, as opposed to 18 cm for the others), and is, in fact, built up from two rolled plates that were welded together by the manufacturer, with much more careful surface preparation to minimize enclosed voids than was needed for the outermost layers. This doubled layer was then cut and machined in two sections in order to provide a straight-through slot (shown in Figs. 1 and 2) toward the primary target downstream in the experimental hall. This slot provides passage for the photon beam during tagger operations, or for electron beams directly into the hall when the tagger system is not in use.

As noted above, the magnet pole tips themselves constitute the lateral walls of the pole-gap vacuum vessel. Stainless-steel vacuum walls were welded directly to the pole root around its entire perimeter. The curved wall along the high-energy edge of the poles incorporates a length of 6.35 cm diameter beam pipe to carry the vacuum path outside the yoke through the straight-ahead slot. The remaining width of this slot to either side of this pipe was filled with solid slabs of magnet iron, tack welded in place during the assembly.

The pole tips, which are also made from AISI 1006 steel, required substantially more precision machine work than any other component. The finished pieces are 15 cm thick, and are both tapered and beveled for optimum field-edge shaping as discussed in Section 3.1 above. A pre-assembly of poles, spine, and inner yoke plates was initially bolted together in order to allow for precise

measurement of the spacing throughout the pole gap, and thus for computation of appropriate shim thicknesses between pole and yoke at each bolt location. The components were then separated and the entire system was re-assembled, this time including the shims, coils, and welded vacuum elements.

The coils are wound from copper conductor having a  $2.54 \times 1.83 \text{ cm}^2$  rectangular section with a central hole 0.953 cm diameter for coolant flow. There are 20 turns on each pole, wrapped with epoxy glass tape for electrical isolation, and arranged in four layers of five turns. Although electrically in series, the separate coolant loops for the four layers are connected in parallel to minimize the pressure drop in the cooling water circuit. At full field (1.75 T, 6.1 GeV), the coils carry a current of 2400 A with a power dissipation of 150 kW.

The focal surface of the magnet, as discussed above, is nearly straight and can be approximated as a plane without affecting the resolution at the order of  $10^{-3} E_0$ . With the radiator foil at the nominal position, the focal plane lies at an angle of  $22.4^\circ$  below the incident beam line, or equivalently  $7.4^\circ$  below the magnet pole chord. Over the dynamic range of photon energies from 20% to 95% of  $E_0$ , this focal plane is more than 9 m in length. The geometry of this arrangement is indicated in Fig. 1.

In order to bring vacuum all the way out to the focal plane, while introducing no obstacle to any degraded electron trajectory over this entire range, we settled upon a welded structure of 0.635 cm thick stainless-steel plate (AISI 304), entirely supported by external ribs, as may be seen in Fig. 3. In the upstream zone (toward the left on the figure), these cantilever loads were shed by welding the support ribs directly to the outer yoke plates of the magnet. Farther downstream, where the focal plane extends well beyond the magnet, it was necessary to wrap the external rib structure all the way around the closed side of the vacuum box, and to stiffen it against buckling failure by means of cross ribs and edge flanges.

The focal plane lies  $\sim 4$  cm beyond, and parallel to, the exit face of the vacuum box. This side of the box is a rectangular flange 1.27 cm thick, of external dimensions  $9.86 \text{ m} \times 91.4 \text{ cm}$ , with a central

rectangular aperture  $961 \times 20 \text{ cm}^2$ . This 20 cm dimension exactly matches the interior dimension of the ribbed portion of the box, which in turn was chosen to match the largest transverse angles of the lowest-energy electrons accepted through the pole gap. The flange is drilled for two bolt patterns – one at the outer perimeter to mate with the light-tight enclosure that supports the detector hodoscope, and a second at the perimeter of the central aperture to accommodate the thin-membrane vacuum window. Its external face is polished over the zone within 15 cm of the lip of the aperture, to provide an appropriate O-ring sealing surface for the window frame.

### 3.3. Field mapping

Extensive mapping of the magnetic field, using the “Ziptrack” [9] apparatus on loan from Fermilab, was performed prior to installation of the tagger magnet in its operating position. In order to allow the effective use of the overhead crane for manipulation of the various heavy components, the magnet was actually assembled lying on its side on the floor of the main experimental hall – i.e. with its symmetry plane horizontal rather than vertical. Mapping in this orientation allowed much more efficient use of the Ziptrack apparatus. Some hardware and software modifications were needed to extend the probe into our comparatively narrow gap, and to allow measurements to be made throughout the crescent-shaped pole gap without danger of collision with the already installed vacuum wall along the curved rear edge of the poles.

The Ziptrack device provides simultaneous mapping of three orthogonal components of the magnetic field with automated probe positioning on a predefinable matrix of points along all three Cartesian axes. The available range of travel during a scan is  $\sim 1.5$  m vertically, and on one horizontal axis, but can be as large as 13 m along the remaining horizontal axis, a feature which made it well suited to our magnet dimensions.

Excitation curves (field vs. current) were mapped at several key points within the field over the full range of the power supply. The Hall-probe sensors on the Ziptrack unit were regularly calibrated against both an NMR probe and a high-precision

Hall probe, using appropriate mechanical jigs to ensure repetitive centering of each probe at exactly the same location in the field.

Once the excitation data had been established, and hysteresis and degaussing effects were understood, a series of extended maps over the entire pole surface, both in and out of the mid-plane, was undertaken using a grid spacing of 2.54 cm parallel to the long pole edge and 1.27 cm in the transverse direction. Data were taken from at least 2.54 cm beyond the full-energy orbit in the pole gap to a distance of 30 cm (approximately five gap widths) outside the pole edge.

Because of vacuum box structure at the two ends of the magnet, extending the Ziptrack measurement grid beyond the pole boundary at the entrance and full-energy exit edges of the magnet was not possible. Measurements along these two axes were taken manually, using a high-precision Hall probe which was moved along a calibrated arm anchored to alignment holes in the magnet. These measurements extended from 50 cm outside the field boundary to 25 cm inside the field, and so extended well into the region of the Ziptrack measurements, with which they were fully consistent.

Field maps were measured for 10 different magnet currents, corresponding to the fields required for incident electron energies from 0.45 to 6.12 GeV. The field maps were stored in the form of two-dimensional arrays suitable for input to the ray-tracing program SNAKE [10]. The additional data points for the entry and full-energy exit regions were not incorporated into the central Ziptrack grid, but instead were used to create separate “field boxes”, a convenient separation for the SNAKE calculation.

When the magnet had been rotated to its final vertical-bending orientation and installed in its gantry, a partial re-measurement of the field was undertaken using a precision Hall probe and a collection of improvised alignment devices inserted into the pole gap from beneath. The re-measured points were consistent with the original map to within 0.2%.

Table 1 shows the basic parameters of the 10 field settings. The incident energy was calculated by ray tracing with the requirement that the full-energy electron beam be deflected by exactly 30°. The

Table 1  
Tagger magnet excitation data

Current (A)	$B_{\max}$ (T)	Incident energy (GeV)
150	0.130	0.449
300	0.257	0.900
600	0.510	1.795
800	0.677	2.388
1000	0.844	2.980
1400	1.174	4.144
1800	1.475	5.189
2000	1.588	5.563
2200	1.682	5.867
2400	1.761	6.120

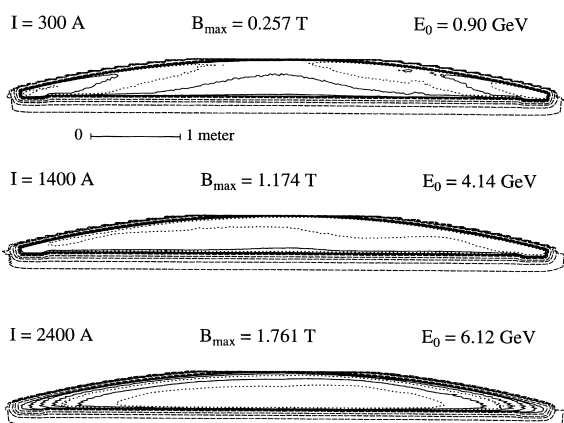


Fig. 4. Field map contour plots for the tagger magnet at three different excitations. Contours are drawn at 99.5%, 99%, 97%, 96%, 95%, 90%, 70%, 50%, 30% and 10% of the maximum field value.

resulting outgoing rays for the 10 field settings coincided to within 1.0 mm. The effective field boundary along the straight edge (calculated by integrating the field from the maximum to the end of the fringe field and dividing by  $B_{\max}$ ) agreed with the POISSON calculations to within 2 mm.

Fig. 4 shows some sample contour plots. The contours at the curved boundary show some spurious structure due to the rectangular grid of the map. The right-angle jogs in the contour along the straight edge are due to the termination of the pole edge chamfer near the two ends. As noted above, this chamfer was not extended all the way to the

ends of the chord so as not to affect the uniformity of the field at the entry and full-energy exit edges.

The uniformity of the field was within 1% over most of the pole area for the settings between 0.51 and 1.48 T, corresponding to incident electron energies of approximately 1.8 and 5.2 GeV. At the higher excitations, a clear falloff of the field near the pole edges was observed, while at very low excitations a small field enhancement appeared near each end. Neither of these features had any significant effect on the calculated energy resolution, and the calculated energy calibration of the focal plane (as a fraction of  $E_0$ ) varied by less than 0.2% between field settings below 1.17 T, increasing to a maximum shift of 1.0% at 1.76 T.

Ray-tracing calculations with SNAKE, using the measured field maps, were used to calculate the energy boundaries of the individual hodoscope scintillators, and the permissible coincidence combinations between the first and second layers of counters. The calculations agreed exactly with counter correlations subsequently observed in the data (see Section 7.2.3 below).

## 4. The hodoscope

### 4.1. Overview and design considerations

The tagger instrumentation must provide two key pieces of information for each detected electron – momentum data of sufficient precision to allow determination of the photon energy to the desired resolution, and timing data adequate to permit the

forming of reliable coincidences with any subsequent events triggered by interaction of that photon in downstream targets. The first of these requires a high degree of segmentation, and hence demands scintillators that are quite small in the dispersive dimension, even on a focal plane that is more than 9 meters in length. The latter calls for output pulse shapes which will allow for precise timing, and hence argues for scintillators which are thick enough to ensure sufficient light for this purpose.

The focal-plane hodoscope, a section of which is sketched in Fig. 5, consists of two separate planes of scintillator detectors. Each detector element is oriented with its working surface normal to the local beam trajectory, the so-called “Venetian blind” geometry. An important benefit of this geometry is that the counters subtend a fairly small angular acceptance for detection of secondary particles that do not come directly from the radiator, especially those generated by slightly degraded electrons which strike the flange and walls of the vacuum chamber adjacent to the full-energy exit port. The two separate planes provide for additional background suppression capability through the use of appropriate logic circuitry to establish geometric constraints on the trajectories of accepted particles.

The first detector plane is called the  $E$ -plane, where  $E$  denotes energy. This plane, used only for momentum definition, lies along the magnet focal surface and contains 384 narrow scintillators (the “ $E$ -counters”). By using an overlapping design, this level of segmentation provides momentum

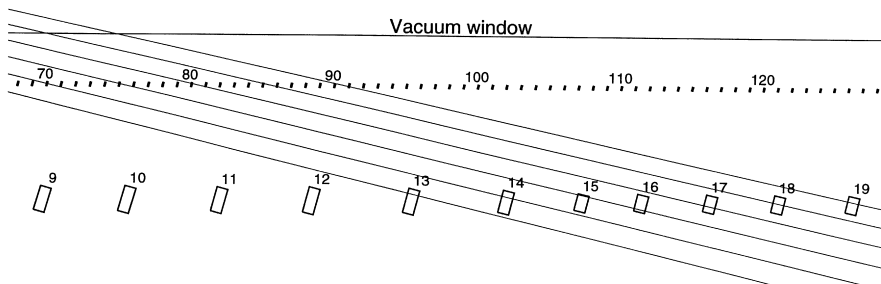


Fig. 5. A scale drawing of a short section of hodoscope with a few typical electron trajectories superposed. Shows the “Venetian Blind” geometry and indicates the general relationship between the  $E$ - and  $T$ -planes of scintillators.

resolution of  $\sim 1 \times 10^{-3}$ , a compromise chosen to reduce cost and complexity while still more than adequate to meet the needs of experiments currently proposed. The intrinsic resolution of the magnet itself is  $\sim 2 \times 10^{-4}$ , and upgrades to this capability of the detector thus remain possible if needed in the future.

The second detector plane (called “*T*” for timing) lies 20 cm behind the *E*-plane (downstream), as measured along the normal to both planes. This plane contains 61 scintillators of considerably larger dimensions which are instrumented to provide the timing precision needed for the coincidence with CLAS.

Electron trajectories cross the focal plane at angles ranging from  $9.5^\circ$  at the high electron momentum (low photon energy) end to  $25^\circ$  at the low-momentum end. Hence the linear distance along the trajectory from plane-to-plane ranges from  $\sim 40$  to  $\sim 120$  cm. The electronic instrumen-

tation of these two detector planes is described in the following sections.

The entire detector hodoscope resides inside a light-tight enclosure suspended beneath the tagger vacuum box. Fig. 6 shows the downstream region of the box opened for service access. The side walls of this enclosure comprise a series of lightweight removable panels made from opaque black plastic, stiffened by expanded metal mesh (which also provides electromagnetic shielding). All panels are interlocked with the high-voltage supplies, both for personnel protection and to prevent phototubes being accidentally energized while exposed to ambient room light. A forced ventilation system, using a small fan unit originally designed for a photographic darkroom, protects against heat buildup when the system is powered.

Structurally, the enclosure is a welded trusswork of aluminum angle members, with sufficient stability to support the full weight of the detectors,

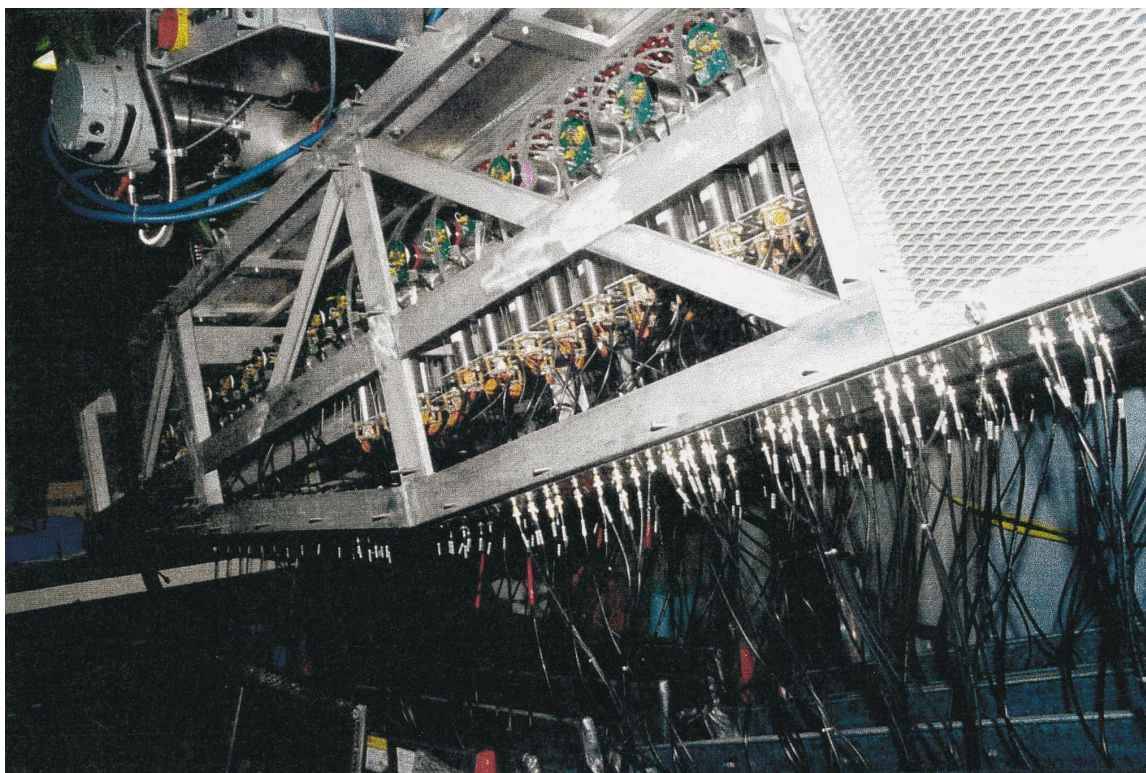


Fig. 6. Color photograph of the detector through an opened service panel. Shows details of box construction, relative locations of detector planes, both sets of phototubes, fiber guides, and several *E*-counters seen in reflection from the vacuum window.

phototubes, and cable segments. In normal operation, this entire load is suspended from a pin-located bolt pattern on the tagger vacuum box. A set of external jacks allows the entire assembly to be withdrawn and then repositioned as an integral unit when necessary to service or replace the vacuum window. The rear (downward-facing) wall has a thin panel in the midplane region to minimize the generation of backscattered background, flanked by solid panels containing all of the signal and high-voltage feedthroughs. The mounting rails for the two detector planes are supported on posts rising from this rear surface.

#### 4.2. The $E$ -plane

The  $E$ -plane is aligned along a flat surface essentially coincident with the optical focal plane of the magnet. These  $E$ -counters record deflected electron positions at the focal surface, and thus the momenta of those degraded electrons. The array is composed of 384 plastic scintillators 20 cm long and 4 mm thick, and with widths (along the dispersion direction) that range from 6 to 18 mm in order to subtend approximately constant momentum intervals of  $0.003E_0$ . Each counter optically overlaps its adjacent neighbors by one-third of their respective widths, thus creating 767 separate photon energy bins through appropriate recording of coincidences and anti-coincidences, and providing an energy resolution of  $0.001E_0$ .

No pulse amplitude data beyond “hit/no-hit” information is required from these small scintillators. We were thus able to realize significant cost savings in the instrumentation of this large set of counters, while still retaining adequate time resolution to support the  $E$ - $T$  coincidence logic discussed in Section 5.3 below. High voltage for the  $E$ -plane is bussed to groups of four tubes, for a significant additional savings in power supply and control costs.

For optimum resolution, the  $E$ -plane must be located close to the exit flange on the tagger magnet vacuum box, in order to minimize the effects of multiple scattering as electrons pass through the thin exit window. Since the  $E$ -plane must lie along the focal surface of the magnet, the vacuum vessel was designed to bring the exit window as close as

practical to this location. The scintillator strips are mounted within 4 cm of the vacuum window frame, supported from below on a system of aluminum rails. This clearance allows for the installation of a layer of metal plates between the  $E$ -plane and the vacuum box for personnel protection when performing service on the detector system while the thin window remains under vacuum load. The small red and white features visible at the top center of Fig. 6 are individual  $E$ -counters, actually seen here in reflection from the thin vacuum window.

Each scintillator is wrapped in one layer of white paper to increase light collection efficiency and to reduce any cross talk between adjacent channels. Optical fiber light guides, seen arcing through the upper section of Fig. 6, carry the signal from one end of each strip to a series of Lucite cylinders,  $\sim 2.5 \text{ cm} \times 2.5 \text{ cm}$ , located well back in the detector enclosure, entirely behind the second detector plane and its phototubes. (These cylinders are hidden behind the central aluminum beam in the photograph.) The fibers pass entirely through an axial hole drilled in each cylinder and are glued in place for mechanical support. The exit face of each fiber/cylinder assembly is polished for optimum optical contact with the photomultiplier tube.

Sufficient light is transmitted via the optical fibers to permit reliable readout with low-cost photomultiplier tubes, clearly visible in the lower portion of the photo. The tubes are held in position against the fiber/cylinder assemblies by a spring-loaded arrangement which allows quick access for replacement and repair. The scintillator strips themselves were cut to specification and polished by the manufacturer (Bicron). All other components in this scintillator/light-guide arrangement were cut, polished, wrapped and assembled locally at Catholic and George Washington Universities.

#### 4.3. The $T$ -plane

To properly associate a tagged electron with the accelerator microstructure (one micropulse each 2 ns into each of the three experimental halls), and thereby with any related downstream event, requires a timing resolution of  $\sigma = 300 \text{ ps}$  or better. The  $T$ -plane provides this information. This plane contains 61 counters, 2 cm thick, read out using

phototubes attached by solid light guides at both ends (transverse to the momentum axis) of each scintillator. These units were shipped by the manufacturer (Bicron) with scintillator and lightguide already integrated. The row of green circuit boards seen in the upper section of Fig. 6 marks the location of the  $T$ -plane tube bases.

The  $T$ -counter scintillators are organized in two groups, with the first group of 19 narrower counters spanning the photon energy range from 75% to 95% of the incident electron energy, and the remaining group of 42 counters spanning the range from 20% to 75%. The  $T$ -counter widths (along the dispersion direction) are varied to compensate for the  $1/E_\gamma$  behavior of the bremsstrahlung cross section, so that the counting rate in each detector remains approximately the same within each group, with the rate in the first group approximately  $\frac{1}{3}$  of that in the second group. The discontinuity in the width progression (visible in Fig. 1) permits operation at considerably higher tagged-photon rates for some experiments which are only interested in the highest-energy photons.

$T$ -counter width acceptances overlap their nearest neighbors by a few mm, just sufficient to ensure that there are no inter-counter gaps through which an electron could escape undetected.

$T$ -counter lengths (transverse to the momentum direction) are also varied from 20 cm at the high electron momentum end to 9 cm at the low-momentum end, tracking the energy dependence of the bremsstrahlung characteristic angle distribution, in order to help suppress potential background from ambient radiation. These lengths were chosen to be large enough to accept  $\sim 98\%$  of electrons from the radiator at  $E_0 = 0.8$  GeV.

## 5. Electronics/readout scheme

The basic logic diagram for the Tagger electronics is shown in Fig. 7. The signature of any event is a set of times from both the  $E$ - and  $T$ -planes, measured with FASTBUS TDCs, which are recorded upon receipt of a valid tagger/CLAS event trigger. These times are subsequently used to

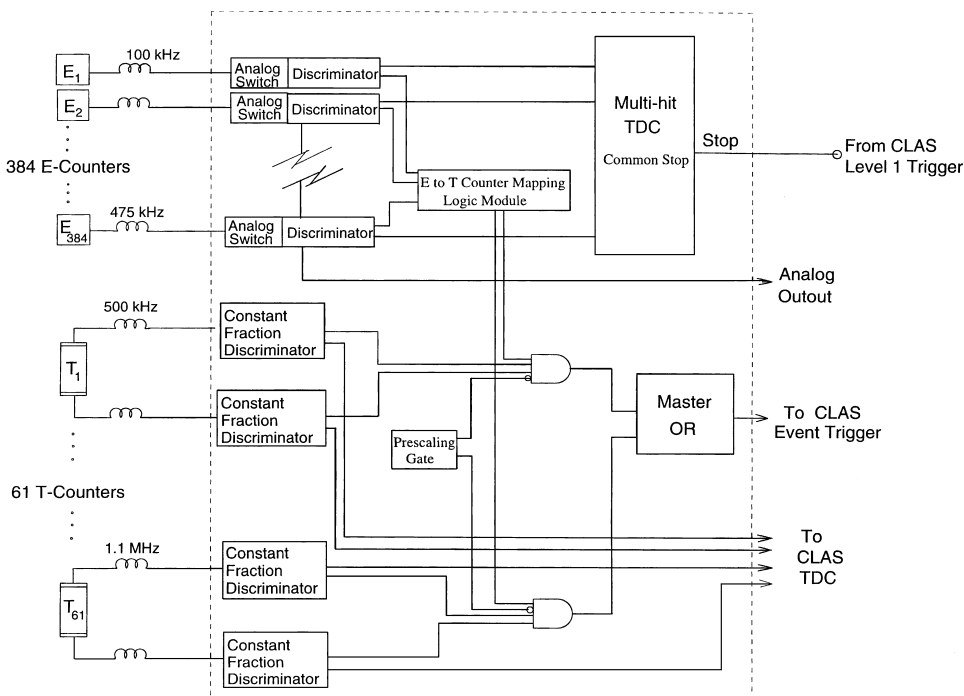


Fig. 7. Schematic of the tagger overall logic design.

determine which counters were hit at the correct time relative to a CLAS trigger to represent a valid event. Appropriate coincidences and counting rates can then all be determined afterward through the use of software.

### 5.1. *T-counter electronics*

Each of the 122 *T*-counter photomultiplier signals is fed to one input of a fast (200 MHz) constant-fraction discriminator (Phillips 715). These discriminators provide output signals for the tagger's own timing system, and also for the photon event logic circuitry that is used to establish a valid tagger photon event.

For the timing system, the output of each fast discriminator is sent to one of four 64-input, 12-bit, multi-hit, FASTBUS TDCs (LRS 1872A), operating in the 50 ps/channel resolution mode. These TDCs are located near the master trigger electronics for the CLAS detector, in racks on the downstream side of the experimental hall. They are operated in common-start mode, with the discriminator signals providing the stops for the individual *T*-channels. Start signals come either from the CLAS event logic, or from one of the beam line photon monitoring devices (see below), depending on whether the event is part of a data collection period or a beam monitoring run. The cables for the discriminator output signals must traverse half-way around the circumference of Hall B to reach these racks, and this provides a delay of 380 ns which is sufficient to get them in time with the CLAS electronics.

For the photon event logic, remaining output signals from the *T*-counter discriminators are used to establish a coincidence between the two photomultipliers which view each individual *T*-plane scintillator. Signals from the left and right ends of each *T*-counter are fed to a fast AND logic unit (Phillips 754). One output of each AND gate is scaled using a 100 MHz scaler (CAEN V560E – not shown in the figure), while another output is used as input to the Master OR.

The Master OR logic is a simple cascade of the outputs of the AND gates into 4-input fast OR gates (Phillips 754). While Fig. 7 shows all 61 *T*-counters included in the logic, the system is easy to

reconfigure to use any multiple of 4 *T*-counters as the Master OR generator. Pick-offs from different levels in the OR gate chain allow for fast identification of the photon energy in the broad energy range covered by signals to that particular OR gate. In fact, the Master OR system has already been replicated for the first 19 *T*-counters, corresponding to the highest photon-energy tagging range (75–95% of the incident electron energy), in order to provide a totally separate signal for an independent experiment running parasitically with the CLAS detector.

The Master OR output provides the signal that a photon has been tagged for the CLAS first-level trigger. It is important that the Master OR signal always arrive at the trigger logic at the same time relative to a photon leaving the radiator, independent of which of the *T*-counters was struck. This relative timing synchronization has been achieved by cutting the cables for each of the 122 *T*-counter signals to the correct length to assure this condition.

The shape of the bremsstrahlung spectrum generates many more tagged lower-energy photons than higher-energy photons, especially when tagging over a large energy range. For the Hall B tagger, the rate in the lowest-energy region of our hodoscope is 4.5 times the rate in an equal width interval in the highest-energy region. Especially when operating with a fairly unrestricted CLAS trigger, this places many more low photon energy events into the data stream, which contributes to the rapidity at which storage media become filled. Moreover, since in many experiments one is primarily interested in events triggered by high-energy photons, this surplus of low-energy events in the trigger could prolong the total experimental running time necessary to generate acceptable statistics in the desired energy range.

To ameliorate this problem somewhat, a system was developed for vetoing the output of the *T*-counter left–right coincidence gates, which allows for the selective prescaling of various segments of the tagging spectrum that is used to generate the photon event trigger. A software controlled VME output register generates the veto signals, with appropriate level conditioning. Control and monitoring software for this system was developed at Arizona

State University. By adjusting the rate and duration of the veto gates, zones of  $T$ -counters can be separately removed from the trigger for different time intervals. The veto gates are typically off for 33 ms, and then on for a time which is an integral multiple of the off time.

A typical veto scheme would divide the hodoscope into four equal zones by photon energy, with the lowest-energy zone being live one-eighth of the time, the next zone one-quarter, the next one-half, and the highest photon energy range operated with no veto. This particular pattern results in a more nearly uniform event rate across the entire photon spectrum (with, in fact, a moderate enhancement for the highest-energy events). The prescale factors are adjustable by software control to meet the needs of particular experiments.

### 5.2. $E$ -counter electronics

Modularized, front-end  $E$ -plane electronics for this apparatus were specifically designed and built at Arizona State University. The output of each of the  $E$ -counter photomultiplier tubes is fed to a signal-amplifier, discriminator, multiplexer and logic module (ADML). The amplifier discriminator in this module is a Phillips 6816, 16-channel, time-over-threshold unit. Eight ADML units are installed in a single custom crate with a dedicated controller module, so three such crates are required for the full complement of 24 modules servicing the 384 photomultiplier inputs from the  $E$ -plane.

The control module in each crate is used to multiplex the photomultiplier signals so that the analog output from any one of the 128  $E$ -counters can be viewed at a single output jack on the front panel. Selection can be made locally via a handheld controller, or remotely via a computer controlled switch, for multiplexing onto a single line for viewing in the experimental hall or in the counting room.

The output from each  $E$ -counter discriminator is fed to one input of a 96-input, 12-bit, multi-hit, FASTBUS TDC (LRS 1877), running in the common-stop mode with a timing resolution of 500 ps/channel. The stop signal is supplied by the CLAS event trigger. The relative time of an event in the  $E$ -counter is used to determine which of the

$E$ -counters were hit during the time bucket of this particular trigger. Because of the  $\frac{1}{3}$  geometric overlap of the  $E$ -plane scintillators, software-determined coincidences between adjacent counters allow subdivision of the 384  $E$ -counter signals into 767 energy channels.

### 5.3. $E$ - $T$ coincidence logic

The timing information from the  $E$ - and  $T$ -counters is used during data analysis to establish the hit patterns and to make tight timing coincidences between the counters. Timing windows of less than 0.5 ns for the  $T$ -counters and 3 ns for the  $E$ -counters allow software rejection of most background events.

All of this final coincidence logic takes place in software after the full CLAS event has been recorded. It was therefore decided to provide an option for some reduction of background events prior to generation of any CLAS trigger signal, by establishing a hardware coincidence between each  $T$ -counter and the group of  $E$ -counters that might be paired with a legitimate electron trajectory through that  $T$ -counter.

Establishing appropriate  $E$ - $T$  coincidences requires dealing with a very complex matrix of overlapping coverage. Each  $T$ -counter is geometrically associated with a group of  $E$ -counters and, because of the angular divergence of the electrons leaving the tagger magnet, many  $E$ -counters can be legitimately associated with adjacent  $T$ -counters. To provide a completely correct logic signal for each of the 61  $T$ -counters would require a matrix logic circuit with 384 inputs.

In order to simplify the coincidence logic process, the ADML units were built to provide logic OR ECL outputs for each contiguous set of eight  $E$ -counters. The coincidence logic matrix ( $E$ - $T$  Logic Unit), built in-house for this purpose, then maps these 48 logic signals from the ADMLs onto the appropriate  $T$ -counter signals. Using the eight-fold logic from the  $E$ -counter array does allow some “false” coincidences between  $E$  and  $T$  pairs that, while relatively close together, are not geometrically correlated with any allowed trajectory. This adds only slightly to the chance background while greatly simplifying the logic matrix.

Each output from the  $E$ - $T$  logic unit is fed to one of the inputs of the AND gate used for each  $T$ -counter. The output gate width of the  $E$ - $T$  logic module is deliberately set to be considerably longer than the outputs from the  $T$ -plane discriminators, so that the timing of the event is still entirely determined by the  $T$ -counter signal.

If desired, the  $E$ - $T$  coincidence requirement can be removed from the trigger logic by setting all the outputs of the  $E$ - $T$  logic unit to the “on” state. This can be done by remote control.

## 6. Other beamline components

### 6.1. Radiator foils

The bremsstrahlung radiator target ladder is based on a modification of a HARP design [11–13] used throughout the CEBAF accelerator as an electron beam position monitor. This modification provides for a longer travel stroke (15.25 cm) which allows the mounting of a standard wire scanner and four radiator targets on the same ladder assembly. Thus, the position of the electron beam can be precisely determined at the exact location where the radiators are to be inserted.

The scanner incorporates a pair of wires, orthogonal to each other but at  $45^\circ$  to the direction of scanning motion, in order to allow two-axis reconstruction of the beam profile. There is no direct readout of any electrical signal from the scanning wires used in the tagger beamline. Rather, the wire functions as a very localized radiator which produces a strong signal of slightly degraded electrons in a set of counters surrounding the beam dump vacuum line. This signal is highly sensitive to the wire position within the incident beam.

Radiators of high atomic number were used in order to minimize the effects from electron–electron bremsstrahlung in the spectrum. Several different thicknesses of radiator targets, ranging from  $1 \times 10^{-6}$  to  $1 \times 10^{-4}$  radiation lengths, have been prepared and mounted at Florida State University. The foils are prepared through deposition onto standard  $2.54 \times 7.62$  cm<sup>2</sup> microscope slides treated

with a release agent consisting of a detergent (Neodol 25-3S from Shell Chemical Company, or Steol CS-460 from Stepan Company) and/or NaCl. The thinner radiators are combination films of gold on a backing of carbon made in one of two methods: (1) carbon deposition by carbon-arc discharge, followed by gold deposition with an electron beam, or (2) carbon and gold both deposited by electron beam in one vacuum cycle. The thicker radiators are free-standing gold films.

Once deposited onto the slide, the films are scored to size and floated in distilled water. The radiator holding frame is then lifted from beneath the film for mounting. The radiator targets are then “slackened” by drawing air across one side of the film to create a pressure differential; this slackening improves the hardness of the films for a longer lifetime. These films then need no special storage environment and can be stored under ambient conditions. Specifications for the radiators which have been produced are given in Table 2.

### 6.2. Beam dump and shielding

The tagger beam dump, designed at Catholic University, must stop all of the full-energy electrons, and must contain the secondary particles created by stopping these electrons, during operation of the tagger system. The shielding around the dump must accomplish two purposes; it must prevent the ground water located outside the dump tunnel from becoming excessively radioactive, and it must shield the CLAS detector system from secondary radiation.

In both of these considerations, it is the neutrons produced inside the dump that are the most penetrating and therefore the most difficult to shield. Ground water activation comes principally from fast neutron spallation reactions. In addition, many lower-energy neutrons are produced from photo-nuclear excitation of the giant resonance. The major source of background for the CLAS comes from neutrons which exit back through the beam transport pipe that carries the electron beam to the dump. Details of the modeling and calculation of these various effects [14], and of the anticipated beam profile in the dump region [15], are available in CEBAF internal publications.

Table 2  
Radiator composition

Radiation length	Composition
$1 \times 10^{-6}$	4 $\mu\text{g}/\text{cm}^2$ Au, on 15 $\mu\text{g}/\text{cm}^2$ C
$2 \times 10^{-6}$	10 $\mu\text{g}/\text{cm}^2$ Au, on 15 $\mu\text{g}/\text{cm}^2$ C
$5 \times 10^{-6}$	30 $\mu\text{g}/\text{cm}^2$ Au, on 15 $\mu\text{g}/\text{cm}^2$ C
$1 \times 10^{-5}$	62 $\mu\text{g}/\text{cm}^2$ Au, on 15 $\mu\text{g}/\text{cm}^2$ C
$2 \times 10^{-5}$	129 $\mu\text{g}/\text{cm}^2$ Au free standing
$5 \times 10^{-5}$	323 $\mu\text{g}/\text{cm}^2$ Au free standing
$1 \times 10^{-4}$	646 $\mu\text{g}/\text{cm}^2$ Au free standing

The design plans for the dump had to take into account the beam power to be dissipated. In the normal, thin-radiator mode of operation this power is quite low, typically a few hundred watts. However, plans had been put forward for producing polarized photons by certain techniques which would require a considerably more intense electron beam. The dump was therefore designed from the beginning to be capable of handling a power level of  $\sim 10$  kW, since it would be prohibitively expensive to retrofit to this capability once any lower-power installation had been completed. This power level is believed to be near the maximum that can be handled with a relatively inexpensive, forced gas flow cooling system for the dump.

The original dump tunnel in the civil construction plans for Hall B is a cylindrical, corrugated iron pipe, 3.05 m in diameter and approximately 12 m long, sloping down beneath the floor at an angle of  $30^\circ$  as indicated in Fig. 3. At its maximum depth the center of the tunnel is 6.1 m below the floor, and almost directly under the CLAS target. The tunnel is surrounded by bedrock, concrete, and construction backfill, but the exact proportions and locations of these materials are uncertain. Nevertheless, since most of Hall B is located below the water table, ground water certainly exists in the environment immediately outside the dump tunnel.

The dump itself is a laminar array in the shape of a 30 cm diameter cylinder. The first section struck by the beam is composed of five discs of graphite (carbon) 10 cm thick and separated by  $\sim 1$  cm air gaps. The rear section is composed of 10 sheets of tungsten 7 mm thick, also with air gaps between.

This array sits within an airtight steel enclosure of 62 cm diameter, with appropriate interior baffling, and with 18.2 cm diameter pipe connections up to floor level, to provide for easy future implementation of forced air flow if upgrade to multi-kilowatt capacity is ever required. The tunnel is entirely filled with iron for 1.5 m downstream of the primary dump, and the central dump enclosure is surrounded by iron  $\sim 1.2$  m thick (radial direction) for an additional 1.3 m (axial).

An inner pipe of diameter  $\sim 1$  m runs from the face of this iron shielding up to floor level, concentric with the original tunnel walls. The space between the two cylinders is backfilled with gravel, and sealed at floor level with poured concrete to a depth of  $\sim 1$  m. The remaining opening is then plugged with another steel can,  $\sim 1.5$  m tall, with penetrations for a central beam pipe  $\sim 25$  cm diameter and for the two airflow pipes previously mentioned. The airflow pipes pass through the can at an angle strongly offset from the axis of the tunnel in order to provide some shadow shielding. The remaining volume of this can is filled with sand. The beam line vacuum extends from the tagger magnet to a stainless steel window just below this can, at which point there is  $\sim 1$  m of sand and/or concrete in direct line between this window and the CLAS.

The beam dump and its associated shielding are very effective. With no radiator, the measured background from the dump while receiving 400 W of power is less than 5 kHz across the entire tagger detector system. Most of these events could probably be eliminated with timing and coincidence checks. Even without any such cuts, this background is less than  $10^{-3}$  of the typical tagging rate.

A much more serious source of background comes from minimally degraded electrons inside the tagger which strike the beam pipe walls, or the tagger vacuum box in the vicinity of the full-energy exit flange, and never make it into the dump tunnel. This background in the tagger hodoscope can be kept well in hand by appropriate timing and coincidence cuts (see Section 7.2.3 below). However, additional lead shielding has been installed in this area, as indicated in Fig. 3, to shadow the CLAS from these components.

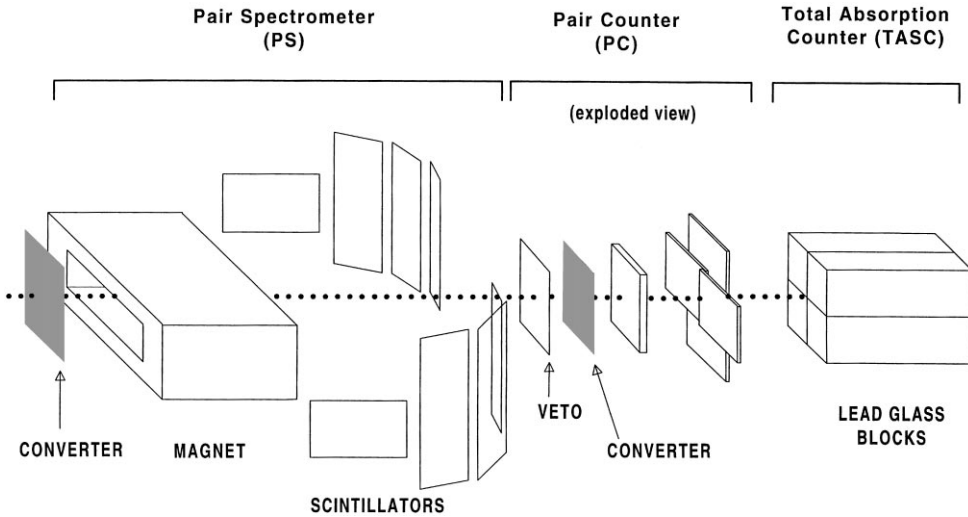


Fig. 8. Sketch showing the general layout of downstream flux monitoring devices (not to scale!)

### 6.3. Flux monitoring devices

Several devices located downstream of the CLAS target, shown in Fig. 8, are used to measure and monitor photon flux. Brief descriptions of the hardware are included in this section. Details of the monitoring algorithm are discussed below in Section 7.2.2.

The most reliable and direct measurement is accomplished with a set of four lead-glass blocks, mounted in a  $2 \times 2$  square array, called the Total Absorption Shower Counter (TASC). This device, constructed and tested by Norfolk State University, is usable only at low rates and is remotely retracted from the photon beam during data runs. The TASC is the primary absolute measure of the photon flux, with close to 100% detection efficiency, and thus, when compared to the sum of all tags in the tagger focal plane, it yields the photon tagging ratio, discussed in more detail in Section 7.2.2.

The lead glass used in the TASC is of type SF3. It is 55% PbO and 45% SiO<sub>2</sub>, with radiation length of 2.36 cm and index of refraction 1.67. The dimensions of each block are  $10 \times 10 \times 40$  cm<sup>3</sup>, for an effective thickness of almost 17 radiation lengths. Each block is read out at one end by a 7.6 cm, Philips XP4312B phototube.

Since the TASC detector cannot handle photon beam rates higher than  $\sim 10^5$  Hz without noticeable degradation, the device is cross calibrated with two other devices – the Pair Spectrometer (PS) and the Pair Counter (PC) – which are able to function at much higher beam intensity.

The pair spectrometer consists of a large aperture dipole magnet and eight scintillator counters – paired four on each side of the beam line. A photon impinging on a thin converter produces  $e^+e^-$  pairs, which are diverged by the magnetic field and then detected in the symmetrically positioned counters. This device is designed to operate at the high photon beam flux ( $5 \times 10^7$  tagged photons/s) of the Hall B facility, and can provide rough energy information on the photon beam.

The housing for the PS converters is a welded box of steel. It has flanges which permit connection to the Hall B vacuum system to support vacuum into the main Hall B dump during electron beam operations. The converters are thin foils of aluminum, 20 cm square. They are held by a three finger spoke holder, also aluminum, which allows for remote insertion of the converter of choice under stepper motor control. Thicknesses of 1% and 2% (radiation lengths) are typically installed, along with a blank slot to allow for free passage of the

beam during electron running. All parts for the vacuum box, converters, and spoke holder were cut and machined in-house at Rensselaer Polytechnic Institute.

The positioning of the scintillator detectors was designed to cover as much of the energy spectrum as possible while overlapping with the Tagger's tagging range. Of the eight scintillators, six were placed with their long dimension vertically, perpendicular to the dispersion plane of the PS magnet. The lowest-energy scintillators were placed with their longest dimension in the dispersion plane in order to fully cover the low end of the Tagger spectrum. The placement of these detector elements can be seen in Fig. 8.

The pair counter, a joint project of Saclay and George Washington, is a much simpler device, intended as a backup intensity monitor to be used with the full beam. It is reliable and easy to maintain and it can remain in the beamline, located between the PS and the TASC, at all times. A thin converter produces electron–positron pairs that are detected in coincidence between a single front scintillator and a rear layer of four, marginally overlapping, scintillators positioned quadrant-wise around the beam centroid. This segmentation of the second layer, together with lateral motion under stepper motor control, provides rough information on the lateral position stability of the photon beam, and also on the beam profile. A veto scintillator is located upstream of the converter to eliminate charged particle background coming from the CLAS. The efficiency of the Pair Counter is roughly 1.5% which, at a beam intensity of  $5 \times 10^7$  photons/s, yields a detection rate of  $\sim 750$  kHz.

The link between the measure of photon flux at low rates and that at nominal data taking beam rates is established by the cross calibration between the TASC and the Pair Spectrometer. The latter device is always in the photon beam just upstream of the TASC. A comparison is made between these devices at lower rates, and the TASC is then removed from the beamline. As the beam intensity is increased, the ratio of the sum of the individual *T*-counter scalers to the PS has been monitored and found to be linear. At high beam rates, the ratio of the “Master OR” (i.e. the single scaler which

counts the logical OR of all *T*-counters) to PC and PS is not linear with beam intensity because of scaler dead time, so individual *T*-counter scalers must be summed off-line to obtain the correct photon-beam intensity.

## 7. Performance to date

### 7.1. Early calibration with beam

The first beam through the tagger system was delivered in December 1996. Between May 1997 and May 1998 the Hall B Photon Tagger was exercised through several testing and commissioning sessions. Of prime concern during this period was the optimization of the timing characteristics of the tagging system. This required the precise time alignment of tagger signals relative to each other, and also relative to the beam RF structure. It was also important to minimize the widths of the time-of-flight spectra, which depend upon the pulse characteristics of the individual PMTs as well as upon the various geometric factors listed above.

Electron beams from 0.9 to 4.0 GeV were used during the commissioning period. These values were determined primarily by the needs of early experiments sharing the beam, and not by consideration of tagger parameters. Most tagger commissioning was done without photon beam collimation in order to be able to measure the full bremsstrahlung beam during photon transmission efficiency measurements.

Relative timing among the *T*-counters, as well as the *E–T* coincidence timing, was verified during the early test runs. *T*-counter cables were adjusted in length to bring *T*-counter relative time differences down to the nanosecond level, so that timing coincidence gate widths could be kept small in order to reduce random background. Timing characteristics are particularly important for the *T*-counters, since the CLAS event trigger is constructed from the Master OR of these counters. It was also important to obtain reasonably good relative timing among *E*-counters so that the hardware *E–T* coincidence logic signals could be formed.

## 7.2. Current status

### 7.2.1. Tagger efficiency

The absolute efficiency of the tagger detector system has not been measured. Because the tagger signal is in the event trigger, tagger efficiency cancels in the ratio of detected to tagger events. Thus the knowledge of the absolute tagger efficiency is not necessary to determine cross sections. However, we believe the absolute efficiency of the tagger is quite high. The pulses produced by a minimum ionizing particle passing through the 2-cm thick  $T$ -counter scintillators provide a spectrum of events that are well separated from the background. The  $T$ -counter discriminators are operated with the threshold set at one-half the value needed to pass essentially all these minimum ionizing pulses, insuring a very high overall absolute efficiency for the tagger.

### 7.2.2. Tagging ratio

The fraction of photons that have been tagged which actually hit the CLAS target is called the Tagging Ratio. This ratio is monitored by inserting the downstream total absorption shower counter (TASC) into the beam. The output of the TASC has been tuned so that all tagged pulses are well above the TASC discriminator threshold, insuring that the TASC efficiency is essentially 100%.

At low photon flux, a tagged photon is defined by a coincidence,  $T_i \cdot \text{TASC}$ , between a signal in the TASC and a signal from any of the  $T_i$  counters in the focal plane. The TDC information for each  $T_i$  and  $E_j$  counter allows determination of the number  $N_\gamma(E_j)$  of tagged photons for each energy channel. The rate of the  $T_i \cdot \text{TASC}$  coincidences and the rate  $T_i^{\text{raw}}$  in the tagger are both measured by scalars. The tagging ratio  $R$  is defined for each  $T$ -channel as being the ratio of these two numbers

$$R_i = (T_i \cdot \text{TASC}) / T_i^{\text{raw}}.$$

If there were no losses of photons, and no spurious background in the tagger, this ratio would be unity.

First estimates of this ratio were made during an early calibration run. Data were obtained using a small auxiliary lead-glass TASC positioned just after an exit window installed directly onto the tagger's straight-through beam pipe, approxi-

ately 8 m from the radiator. Except for low  $T$ -counter numbers, corresponding to the highest photon energy, the ratio was approximately 98%. The measured ratio cannot be unity since the tagger has finite acceptance for Møller scattered electrons, where no photon is created. Such events contribute to the number of tags ( $N_\gamma$ ) without generating any event in the TASC, and this effect was indeed seen in this early calibration data as a falloff in the measured ratio for the highest photon energies (corresponding to low  $T$ -counter numbers).

Fig. 9 displays the tagging ratio as a function of  $T$ -counter number from a later measurement using the permanent downstream TASC detector, located  $\sim 50$  m from the radiator. It shows a measured tagging ratio of about 78%, which is typical for photon energies over most of the upper operational range – consistent with the expected additional losses due to target, air, and beam pipe windows between the radiator and the permanent TASC. A plastic bag filled with helium is installed during photon beam operations between the CLAS target and the downstream devices to help reduce such losses (GEANT simulation indicates a correction of  $\sim 3\%$ ). The collimation system, which is

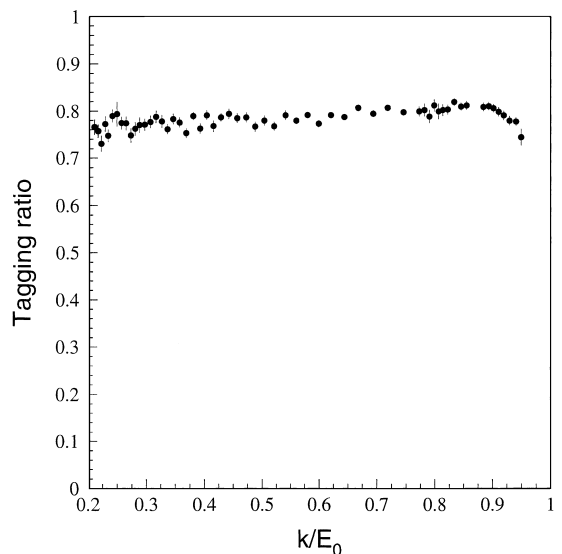


Fig. 9. Plot of the “tagging ratio” (defined in Section 7.2.2) for individual  $T$ -counters vs. fraction of incident energy.

designed to limit the beam to a diameter of 33 mm at the CLAS target, accepts a cone of half-angle 0.74 mr. This corresponds to  $2.4\theta_c$  at 1.6 GeV incident energy, and reduces the overall ratio to about 75% at this lower end of the operational range. The tagging ratio depends strongly on the beam set-up through the accelerator and switchyard, and variations of  $\sim 5\%$  have been detected. Thus, it must be regularly monitored.

The Pair Spectrometer efficiency  $\varepsilon_{\text{PS}}$  is measured at low intensity by comparison with the TASC

$$\varepsilon_{\text{PS}} = (T_i \cdot \text{PS}) / (T_i \cdot \text{TASC})$$

where  $T_i \cdot \text{TASC}$  and  $T_i \cdot \text{PS}$  stand for the number of coincidences between a  $T$ -counter and the TASC or the PS, respectively. These numbers are recorded on scalers. This measurement is done at low intensity during a “normalization run”. At high intensity, i.e. during a “production run”, the TASC is removed from the beam line and only the number of  $T_i \cdot \text{PS}$  coincidences (true and accidental) are recorded. The number of photons during a production run,  $N_{\gamma}^{\text{prod}}(E_j)$ , is then simply deduced from the number of photons measured during a normalization run,  $N_{\gamma}^{\text{norm}}(E_j)$ , as

$$N_{\gamma}^{\text{prod}}(E_j) = N_{\gamma}^{\text{norm}}(E_j)\eta$$

where

$$\eta = (T_i \cdot \text{PS})^{\text{prod}} / (T_i \cdot \text{PS})^{\text{norm}}.$$

The ratio  $\eta$  is a constant proportional to the number of incoming electrons, and takes into account any variation of the tagging ratio. It is expected to be independent of  $T$ -counter number (and hence is not subscripted) as long as there is no variation within the electronics between the normalization and the production runs. A normalization run is performed every day during an experiment to ensure that  $\varepsilon_{\text{PS}}$  does not vary.

### 7.2.3. $E$ - and $T$ -counter correlation

The dual planes of detectors, the  $E$ - and  $T$ -counters, are arranged such that electrons coming from the radiator can pass through a restricted set of allowed pairs of scintillators. The arrival time data can be scanned for allowed pairs and for disallowed pairs coming from background and random noise events. The allowed pairs of detectors

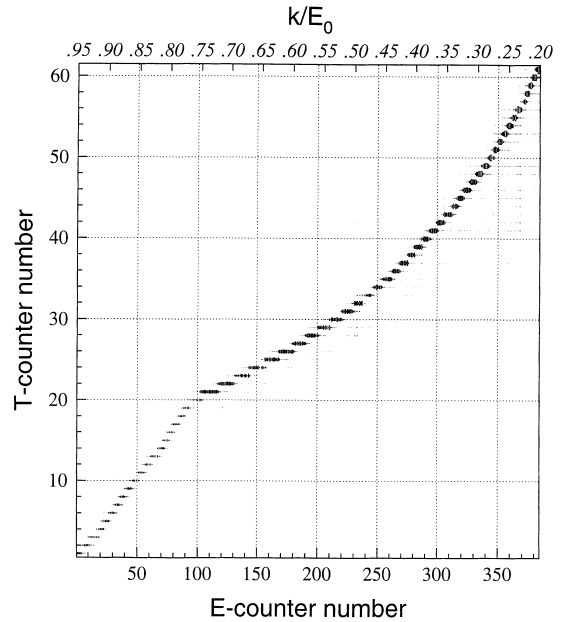


Fig. 10. Cluster plot of  $T$ -counter hits vs.  $E$ -counter number. (Size of each plotted box represents number of events. That detail is not easily seen at this scale, but is also not critical to the conclusions being drawn.) Shows the correlation between the  $E$  and  $T$  hodoscope planes.  $E$ -counters are sized to represent a constant momentum bite, so horizontal scale is linear in photon energy.

were determined from a calculation of possible electron orbits using the magnetic field maps and the measured positions of the detectors. A display of the number of detected events in the  $T$ -counters as a function of  $E$ -counter number is shown in Fig. 10. The agreement between the calculated and observed hit pattern is excellent, indicating that we have good knowledge of the magnetic field and the detector placement. In this figure the  $x$ -axis, representing  $E$ -counter number, is linear in electron energy. The  $y$ -axis, the  $T$ -counter number, is not linear in energy. The ridge of maximum number of events shows the discontinuity in slope caused by the finer gradation of the first 19  $T$ -counters, followed by the curving section caused by the progressive narrowing of the remaining  $T$ -counters to maintain constant counting rate in a rising bremsstrahlung spectrum.

Any events which are not in the vicinity of the maximum ridge are due to background. One can

see that the overall background is quite small, and that it is more significant near the lower photon energy portion of the spectrum. The additional background in this region is thought to be due to untagged bremsstrahlung electrons that have lost enough energy to strike the vacuum pipe or flange at the exit of the tagger vacuum chamber, located just above the low photon energy end of the detector hodoscope. Background from these events will clearly be coming from the wrong direction and will not strike properly correlated detectors. It will therefore be straightforward to eliminate these events from the analysis.

#### 7.2.4. Event timing

The time of arrival of an event is determined very precisely from a combination of the time signals from each end of the  $T$ -counter. With the measurement of both times, the time jitter from the approximately 1.4 ns variation in the light transit time, caused by the lateral spread in the electrons, can be eliminated. The sum of the times from the left and right ends of the scintillators includes the total light drift time, independent of the starting point in the scintillator, and thus is a constant.

We have timed these signals against a signal received from the RF drive of the accelerator. Fig. 11 shows the timing spectrum thus generated. The timing resolution obtained is approximately

110 ps for  $1\sigma$ , greatly exceeding the design goal of 300 ps for this quantity. This is by far the tightest time resolution in the system, and allows us to uniquely identify the RF beam bucket responsible for initiating an event, and essentially eliminates the uncertainty in start time used for time-of-flight measurements in CLAS. The figure clearly shows the 2 ns microstructure of the CEBAF beam. Interestingly, the figure also shows that with the accelerator tune employed for these measurements there is a small spill from the million times more intense interspersed beam being sent to another experimental hall – the small peak located at two-thirds of the spacing (1.33 ns) between the peaks produced by the main beam entering Hall B.

#### 7.3. Conclusion

The JLab photon-tagging system has satisfied its design objectives. It meets, and frequently exceeds, the capabilities required in order to achieve the physics goals of any real- photon experiment so far approved for Hall B at Jefferson Lab. At the time of this writing, we are nearing the end of the first year of data collection with this facility. Early analyses look very encouraging, and presentation of preliminary physics results at professional meetings has already begun.

#### Acknowledgements

The list of people who could be thanked at the end of a project of more than five years duration becomes all but unmanageable, but the contributions of the following individuals in particular are gratefully acknowledged: Addison Lake, John O'Meara and John Robb of the JLab engineering staff for their invaluable participation in all stages of the design and assembly process; Bernhard Mecking and Arne Freyberger of JLab, and Dave Doughty of Christopher Newport University, for many helpful suggestions and contributions throughout the extended lifetime of this project; Paul Branch of CUA for his machinist skills during the prototyping phase; Irwin Price of GWU for essential financial support to one of us (WJB); Randall Stevens and Aaron Vanderpool of ASU for technical assistance in fabricating and testing

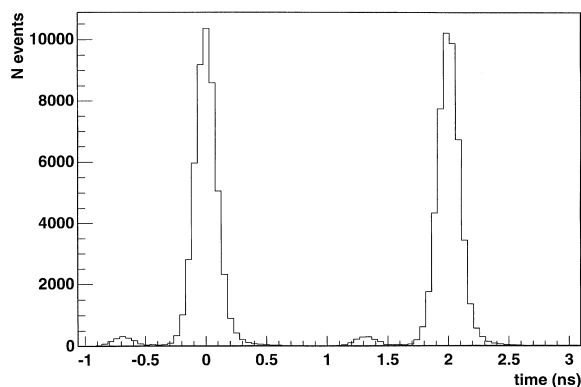


Fig. 11. Tagger timing spectrum, showing the timing resolution of the tagger  $T$ -plane. The 2 ns interval between beam “buckets” into Hall B is indicated. The small intervening peaks, located at  $2/3$  of this 2 ns spacing, represent spill from “buckets” being delivered to one of the two adjacent Experimental Halls.

tagger electronics; R. DiBari, K. Knowles and R. Thomas of RPI for technical contributions to the Pair Spectrometer; Scott Teige of Indiana U. for providing the lead glass blocks for the TASC, and Pete Hemler of JLab for designing its support structure; Powell Barber of FSU for his expertise in manufacturing the thin radiator targets, and Robin Chappell and the FSU machine shop for fabricating the HARPs; Doug Tilles and the entire JLab Hall B crew of riggers and welders for cheerful and reliable day to day support during installation and calibration; Students Henrik Ayvazian, Zoran Bucalo, Juan Carlos Sanabria, Bryan Carnahan, Catalina Cetina, Katherine Keilty, Aziz Shafi, Michele Schottenbauer, and Michael Wood, and technician Shane Briscoe, for their participation in construction and testing. This project was supported in part by the National Science Foundation (ASU, CUA, FSU, RPI) and by the Department of Energy (GWU, JLab).

## References

- [1] V.D. Burkert, B.A. Mecking, in: B. Frois, I. Sick (Eds.), *Modern Topics in Electron Scattering*, World Scientific, Singapore, 1991.
- [2] J.D. Kellie, I. Anthony, S.J. Hall, I.J.D. MacGregor, A. McPherson, P.J. Thorley, S.L. Wan, F. Zetl, *Nucl. Instr. and Meth. A* 241 (1985) 154.
- [3] I. Anthony, J.D. Kellie, S.J. Hall, G.J. Miller, J. Ahrens, *Nucl. Instr. and Meth. A* 301 (1991) 230.
- [4] P. Detemple, K.H. Althoff, G. Anton, J. Arends, A. Bock, M. Breuer, K. Büchler, G. Nöldeke, M. Serwazi, W. Schneider, D. Urban, B. Zucht, *Nucl. Instr. and Meth. A* 321 (1992) 479 and works cited therein.
- [5] S.K. Matthews, Hall Crannell, J.T. O'Brien, D.I. Sober, *Nucl. Instr. and Meth. A* 421 (1999) 23.
- [6] D.I. Sober, *A Guide to the Optics of the Tagged Photon Magnet*, CLAS Note 91-012.
- [7] J. Borggreen, B. Elbek, L.P. Nielson, *Nucl. Instr. and Meth.* 24 (1963) 1.
- [8] *Poisson/Superfish Reference Manual*, Los Alamos Accelerator Code Group, LA-UR-87-126, 1987.
- [9] *ZIPTRAK Operations Manual*, Fermilab Survey Group, private communication.
- [10] Pascal Vernin, private communication.
- [11] C. Yan et al., *Nucl. Instr. and Meth. A* 365 (1995) 261.
- [12] R. Abbott, B. Bowling, E. Woodworth, *HARP User's Manual*, CEBAF Tech Note TN92-050, 1992.
- [13] J.E. Feldl, private communication.
- [14] Hall Crannell, *Considerations for the Design of the CLAS Tagger Beam Dump*, CLAS Note 93-023.
- [15] D. I. Sober, *Tagger Electron Beam Dump Considerations*, CLAS Note 92-013.